Available online at www.eccomasproceedia.org
Eccomas Proceedia EUROGEN (2023) 180-188

ECCOMAS
Proceedia

EUROGEN 2023
15th ECCOMAS Thematic Conference on
Evolutionary and Deterministic Methods for Design, Optimization and Control
N. Gauger, K. Giannakoglou, M. Papadrakakis, J. Periaux (eds.)
Chania, Crete Greece, 1–3 June 2023

TOWARDS REAL-TIME CFD

Anirudh N. Rao[1,2], Sina C. Stapelfeldt[1], Andrew Duncan[3], Shahrokh Shahpar[4] and Francesco Montomoli[2]

[1]Vibration UTC, Department of Mechanical Engineering,
Imperial College London, South Kensington, London, UK SW7 2BX
[2]Department of Aeronautics, Imperial College London, South Kensington, London, UK SW7 2BX
[3]Faculty of Natural Sciences, Department of Mathematics, Imperial College London, South Kensington, London, UK SW7 2BX
[4]Innovation Hub, Future Methods, Rolls-Royce plc, Derby, UK, DE24 8BJ
Corresponding author's email: anirudh.rao@imperial.ac.uk

Abstract. *Quick turnaround times in the design stages of the aerospace industry require faster and more accurate predictions of the flow fields, especially in turbomachinery applications. Recent advances in machine learning combined with the increased computational resources available, data-driven approaches are replacing or aiding expensive computational fluid dynamics (CFD) simulations. Here, an unsteady flowfield from an aspirated intake subjected to a crosswind is used to delineate the flow features using image segmentation, where a convolutional neural network (CNN) is used. Preliminary results from the comparison of two CNN architectures are compared to identify regions of intake distortions such as the ground vortex or a lip separation. Future work will be focussed on using these architectures to predict CFD flow topologies, which will allow the rapid assessment of geometric changes at the design stage, and substantially improve the overall time required in the performance evaluation of turbomachinery components.*

Keywords: Convolutional neural network, UNET, intake flows, distortion

Peer-review under responsibility of the organizing committee of EUROGEN 2023.
doi: 10.7712/140123.10198.18946

1 INTRODUCTION

Machine learning techniques have gained popularity in recent years with deep learning techniques applied to computational fluid dynamics (CFD) processes in the turbomachinery and aviation industries [1]. These machine learning algorithms have been used to augment lower-fidelity CFD models such as URANS (unsteady Reynolds–Averaged Navier–Stokes) with data obtained from high-fidelity CFD models such as LES (large eddy simulation) to train the machine learning models, primarily with the aim to improve the modelling of turbulence. More recently, convolutional neural networks (CNN) which are a class of deep neural networks, have been used to predict the flow fields, and the lift and drag coefficients of airfoils for flow control applications accurately ([2], [3]). Using a limited number of airfoil geometries and flow conditions, Bhatnagar et al. [3] and Thuerey et al.[4] demonstrated that they were able to predict the flow field and fluid quantities faster than RANS simulations for unseen airfoils with a root mean square error of less than 10% across the flowfield. These deep learning methods usually involve the use of UNET-type architectures involving an encoder and a decoder path. These architectures have been used for the prediction of real-time flow solutions for hydrodynamic applications ([5]).

UNET is a fully convolutional neural network architecture that was developed for biomedical image segmentation [6, 7] with a small dataset of images. The UNET architecture consists of a contracting path and an expansive path resulting in a u-shape and giving the architecture its name. At each level, there are two convolution operations followed by a rectified linear unit (ReLU) operation and a max-pooling operation. The images are down-sampled in the contracting path while the feature information is increased. On the decoder side, the transpose of these operations is performed at each level. At each up-sampling level, the feature map from the corresponding contracting level is concatenated and these are known as skip connections. These skip connections provide high-resolution features to improve the performance of these networks. The resulting output from the UNET architecture is a highly segmented map and these are useful in biomedical imaging [8, 9]. Following the success of UNET, a range of UNET architectures have been proposed (see [10]). Of these, UNET++ is purported to have an overall gain over the conventional UNET architecture [11]. UNET++ consists of an encoder and decoder sub-networks that are connected through a series of nested, dense skip pathways with multiple convolutional blocks in between. The high-resolution feature maps from the encoder network are enriched prior to concatenation with the corresponding semantically rich feature maps from the decoder network, which in turn capture a finer foreground image compared to the background [11].

In this study, we consider the results from a simplified aspirated intake geometry in ground proximity, which has recently been used to validate CFD codes [12]. The intake is subjected to crosswinds and a range of flow topologies are observed at the Aerodynamic Interface Plane(AIP). Quantifying the losses at the AIP is significant from an aero-mechanical perspective, as the frequencies associated with the distortion can have an impact on the forced response characteristics of the downstream turbomachinery components. At low crosswind velocities, a ground vortex forms which is ingested into the intake and at high crosswind velocities, the vortex begins to oscillate leading to unsteady dynamics and larger distortion levels compared to lower crosswind velocities. At higher crosswind velocities, lip separation is observed leading to a larger pressure loss at the AIP. The flow dynamics for this generic intake configuration provide a range of CFD flow topologies from the unsteady dynamics and thus a rich dataset of CFD images.

The remainder of this paper is organised as follows: section 2 deals with the numerical

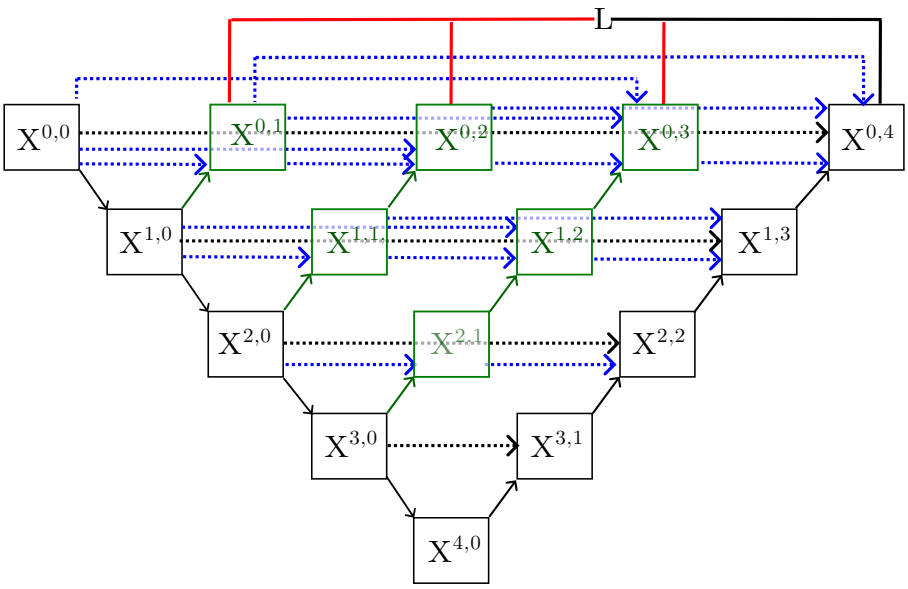

Figure 1: Schematic of the UNET and UNET++ architectures based on Zhou et al.[11]. Black blocks indicate the original UNET architecture, green and blue show dense convolution blocks on the skip pathways, and red indicates deep supervision. Red, green, and blue components distinguish UNET++ from UNET.

method used to generate the numerical data for the CFD simulations. Section 3 describe the flow topology and the losses observed in an intake flow in ground proximity and the comparison of the two UNET architectures used for semantic segmentation. This is followed by conclusions in section 4.

2 NUMERICAL SETUP AND SOLVER

The geometry chosen for this study is the simplified intake proposed at the 5^{th} Propulsion and Aerodynamics workshop [13] in January 2020, and is based on the experimental and numerical studies from Cranfield University [14, 15, 16, 17]. The cross-sectional view of the intake is shown in Fig. 2(a). The intake lip has a 2:1 elliptical profile and the AIP/fan-face is located $0.7D_i$ downstream of the intake highlight plane. The length of the intake is $8.4D_i$ and the intake exit boundary is approximately $7.7D_i$ downstream of the intake lip. For the CFD simulations in this study, the intake was placed in a computational domain which was $48D_i$ in length as measured from the start of the inlet to the exit boundary, $30D_i$ in width and $15D_i$ in height (figure 2(b)). The intake was placed $0.25D_l$ above the ground plane. The Reynolds number was set to $\simeq 1\times10^6$ based on the intake diameter (D_i) and the intake velocity U_i. The intake exit boundary was set as a mass flow boundary condition with an intake mass flow rate of $\dot{m}$=1.46kg/s, and the corresponding value of the fan-face Mach number was $M_{AIP} = 0.55$ or the equivalent capacity $Q = 0.0332$. The non-dimensionalised velocity U^* is defined as the ratio of the intake velocity (U_i) to the crosswind velocity (U_∞). The left-hand face (looking upstream of the intake) was assigned a velocity inlet boundary condition and the right-hand face was assigned the outlet boundary, and the remaining boundaries were assigned a symmetry boundary condition.

A three-dimensional time-accurate finite volume numerical solver (AU3D), was employed to

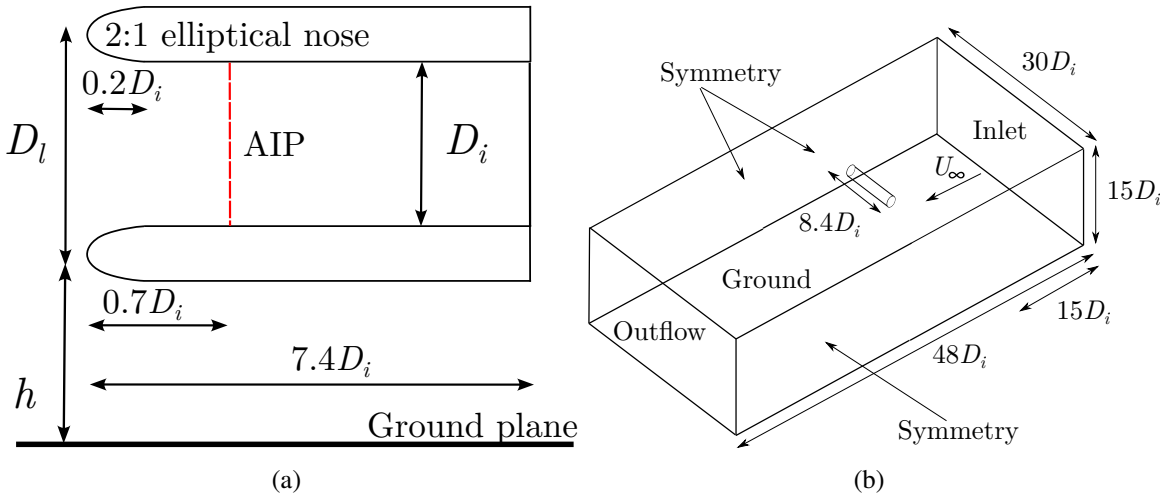

Figure 2: (a) Cross-sectional view of the axisymmetric intake with an elliptical lip showing the major dimensions of the intake in terms of the intake diameter (D_i). The intake is located at a height $h/D_l = 0.25$ from the ground plane. Image reproduced from the PAW participant guide [13]. (b) The dimensions of the computational domain used, with the flow from the left-hand side of the intake.

solve the Favre-averaged Navier–Stokes equations, which has been developed at Imperial College London together with Rolls Royce plc [18, 19]. The code uses a time implicit algorithm which is second-order accurate in both space and time. The turbulence model used was a standard Spalart-Allmaras model implemented in the code. The numerical solver is capable of simulating both steady and unsteady flows, and has been widely used to perform aero-mechanical computations involving flows in turbomachinery and aero-engine intakes [20, 21, 22].

3 PRELIMINARY RESULTS

3.1 Flow Topology

For the intake subjected to a low crosswind ($U^* \gtrsim 15$), a ground vortex is ingested into the intake with a vortex forming on the windward side at approximately a 5 o'clock position at the Aerodynamic Interface plane. As the crosswind velocity is increased, the ingested vortex begins to oscillate periodically. The magnitude of the distortion of the vortex varies as it oscillates ($13 \lesssim U^* \lesssim 6$) with the vortex appearing on the leeward side at reduced strength. For high crosswind velocities ($U^* \lesssim 6$), a windward side lip separation is observed together with the ground vortex and for even higher crosswind velocities of $U^* \lesssim 4.55$, the ground vortex is transformed to a trailing vortex and a distinct vortex does not form at the AIP. The distortions measured at the AIP were within the range of values observed by various researchers at the 5^{th} Propulsion and Aerodynamics workshop [22]. In this study, we consider two crosswind conditions, one at $U^* \simeq 6.1$ and the other at $U^* \simeq 5.25$. The former shows only the presence of a ground vortex and the trailing vortex at approximately 10-12 o'clock position, while the latter shows a large windward lip separation. These simulations were run for several through-flows post-transience, and the intake pressure recovery ($IPR = P_o/P_{o,\infty}$) at the AIP was monitored. The distortion metrics were aperiodic and this was primarily associated with the meandering of the ground vortex.

Figure 3 shows the contours of IPR at the AIP for the two crosswind conditions investigated. For $U^* \simeq 6.1$, the ground vortex oscillates between the 5 and 7 o'clock positions at the AIP

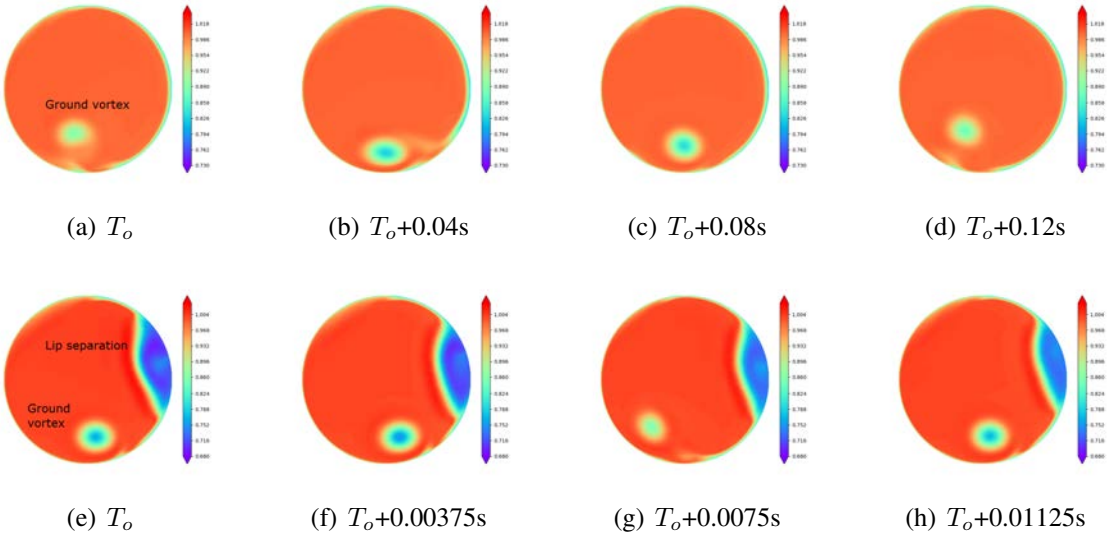

(a) T_o (b) T_o+0.04s (c) T_o+0.08s (d) T_o+0.12s

(e) T_o (f) T_o+0.00375s (g) T_o+0.0075s (h) T_o+0.01125s

Figure 3: Contours of IPR at the AIP at the specified time-instants for (a)-(d): $U^* \simeq 6.1$; where the contour limits are between 0.073 (blue) and 1.018 (red); and (e)-(h): $U^* \simeq 5.25$, where the contour levels are between 0.68 (blue) to 1.004 (red). For $U^* \simeq 6.1$, only the ground vortex is observed at the AIP and for $U^* = 5.25$, a windward side lip separation is observed along with the ground vortex. Flow is from left to right in these images.

with the distortion levels varying over this time period. At the higher crosswind velocity of $U^* \simeq 5.25$, the lip separation is observed with the ground vortex occasionally meandering to the leeward side. The shape and size of the lip separation vary with time. For the higher crosswind condition, the distortion is higher on account of the lip separation leading to a large loss in $P_{o,\,AIP}$. Over the course of these two simulations, there are variations in the total pressure loss at the AIP resulting in a rich dataset of images for the training using a convolution neural network for each crosswind condition. The snapshots for $U^* \simeq 6.1$ and 5.25 were spaced $3.75\times10^{-}4$s and $7.5\times10^{-}5$s apart.

3.2 Image segmentation

For the image segmentation, the images of total pressure contours from the two URANS simulations above were captured at the AIP. The images were then scaled to 512×512 pixels and converted to grayscale. The ground truth or the masks were generated by inverting these images to obtain a black-and-white image of the same dimension. The objective of the work is to discern the region of total pressure loss such as the ground vortex or the windward side lip separation (Fig. 3) from the flow field and the masks provided a fairly accurate representation of the regions of distortion. Images in each set were then categorised into training, validation and test datasets. Two architectures of the UNET family were used; first, the default UNET architecture, and the second, UNET++, which has multiple encoders to generate strong features from the input image. For the purposes of this study, openly available codes for UNET ([23] and UNET++ architectures ([24]) were used. The hyperparameters - batch size and epochs used for the comparison of the two cases were 10 and 20, respectively. The same number of training, validation and test images were used for a direct comparison between the two architectures and are listed in Table 1. For the image sizes specified, the UNET architecture took approximately one hour while UNET++ took approximately six hours due to its dense skip connections running on sixteen CPU's with an average use of 25GB of RAM.

Table 1: Topology of the UNET architecture used in Data Set Training and Testing.

U^*	**Training data size**	**Validation data size**	**Testing data size**
6.1	1000	50	50
5.25	2500	100	100

Fig. 4 shows the comparison of the two architectures in relation to the ground truth and the original grayscaled image of the total pressure contour of the AIP for $U^* \simeq 6.1$ and 5.25. A random image from the test dataset was chosen for the back-to-back comparison of the two architectures. For both crosswind conditions, UNET seems to closely predict the features of the vortex features such as the separation along the shroud (Fig. 4(c)), and the entire extent of the vortex is captured well with UNET. In contrast, UNET++ typically captures a smaller region of the vortex or the lip separation (Fig. fig:1d and 4(h)) and also captures the centre of the vortex which is represented by a darker colour (the deeper shade of blue as seen in the colour images in Fig. 3(c)).

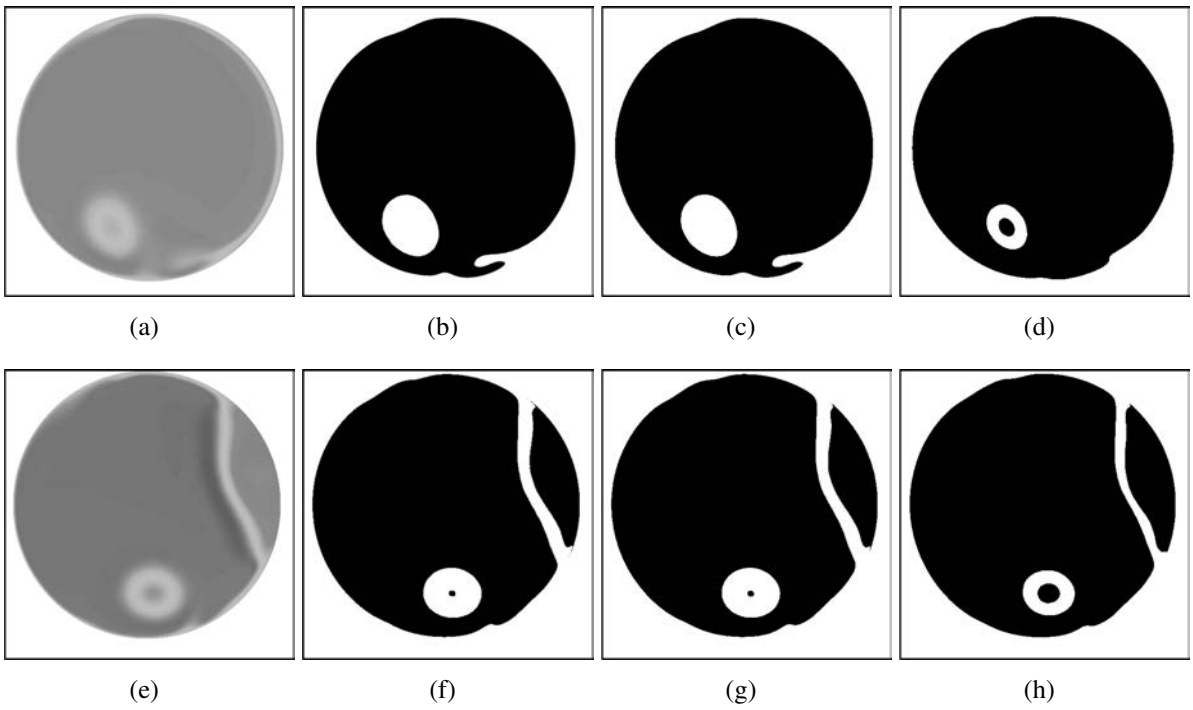

Figure 4: Comparison of the outcomes of the two UNET architectures for a random instantaneous snapshot of the total pressure contours at the AIP. (a),(e) Gray-scaled contour of the total pressure contours. (b), (f) The corresponding ground truth or mask used. (c), (g) the predicted output from UNET and, (d),(h) the predicted mask from UNET++. Top row: $U^* \simeq 6.1$; bottom row: $U^* \simeq 5.25$. Flow is from left to right in these images. The intake lip separation is observed on the windward side for $U^* \simeq 5.25$.

Thus, the two UNET architectures are successfully able to predict the segmentation of the flow features from the background and qualitatively demarcate the regions of distortions.

4 CONCLUSION AND FUTURE WORK

In this study, a simplified aspirated intake was used as a test case to investigate the flow dynamics when subjected to a crosswind. The rich dataset generated from the flow simulations provides a host of images which were used for semantic segmentation using UNET and UNET++ architectures. The images from the CFD simulations were trained using the two architectures and small differences pertaining to the size of the distortion were observed. Further investigations are currently underway to optimise the number of training images/epochs required for the accurate segmentation of such images. Future work is aimed at developing fluid dynamic predictions based on UNET architectures [5, 25, 26, 27].

Acknowledgements

This study is supported by the NEXTAIR project which has received funding from the European Union's Horizon Europe research and innovation program under grant agreement No. 101056732. The authors would also like to acknowledge the financial support from Innovate UK grant number 46511 for the simulation carried out under the FANFARE project. The authors would like to thank Rolls Royce plc for providing access to the numerical solver and for allowing the publication of this work. Lastly, the authors also acknowledge the computing resources provided by Imperial College London, UK.

Views and opinions expressed are however those of the author(s) only and do not necessarily reflect those of the European Union. Neither the European Union nor the granting authority can be held responsible for them.

REFERENCES

[1] Hammond, J., Montomoli, F., Pietropaoli, M., Sandberg, R. D., and Michelassi, V., 2022. "Machine Learning for the Development of Data-Driven Turbulence Closures in Coolant Systems". *Journal of Turbomachinery,* ***144***(8), 03. 081003.

[2] Portal-Porras, K., Fernandez-Gamiz, U., Zulueta, E., Ballesteros-Coll, A., and Zulueta, A., 2022. "CNN-based flow control device modelling on aerodynamic airfoils". *Scientific Reports,* ***12***(1), May, p. 8205.

[3] Bhatnagar, S., Afshar, Y., Pan, S., Duraisamy, K., and Kaushik, S., 2019. "Prediction of aerodynamic flow fields using convolutional neural networks". *Computational Mechanics,* ***64***(2), Aug, pp. 525–545.

[4] Thuerey, N., Weißenow, K., Prantl, L., and Hu, X., 2020. "Deep learning methods for reynolds-averaged navier–stokes simulations of airfoil flows". *AIAA Journal,* ***58***(1), pp. 25–36.

[5] Hou, Y., Li, H., Chen, H., Wei, W., Wang, J., and Huang, Y., 2022. "A novel deep U-Net-LSTM framework for time-sequenced hydrodynamics prediction of the SUBOFF AFF-8". *Engineering Applications of Computational Fluid Mechanics,* ***16***(1), pp. 630–645.

[6] Ronneberger, O., Fischer, P., and Brox, T., 2015. U-net: Convolutional networks for biomedical image segmentation.

[7] Shelhamer, E., Long, J., and Darrell, T., 2017. "Fully convolutional networks for semantic segmentation". *IEEE Transactions on Pattern Analysis and Machine Intelligence,* ***39***(4), pp. 640–651.

[8] Falk, T., Mai, D., Bensch, R., Çiçek, Ö., Abdulkadir, A., Marrakchi, Y., Böhm, A., Deubner, J., Jäckel, Z., Seiwald, K., Dovzhenko, A., Tietz, O., Dal Bosco, C., Walsh, S., Saltukoglu, D., Tay, T. L., Prinz, M., Palme, K., Simons, M., Diester, I., Brox, T., and Ronneberger, O., 2019. "U-net: deep learning for cell counting, detection, and morphometry". *Nature Methods,* ***16***(1), Jan, pp. 67–70.

[9] Saood, A., and Hatem, I., 2021. "Covid-19 lung ct image segmentation using deep learning methods: U-net versus segnet". *BMC Medical Imaging,* ***21***(1), Feb, p. 19.

[10] Siddique, N., Paheding, S., Elkin, C. P., and Devabhaktuni, V., 2021. "U-net and its variants for medical image segmentation: A review of theory and applications". *IEEE Access,* ***9***, pp. 82031–82057.

[11] Zhou, Z., Rahman Siddiquee, M. M., Tajbakhsh, N., and Liang, J., 2018. "UNet++: A Nested U-Net Architecture for Medical Image Segmentation". In Deep Learning in Medical Image Analysis and Multimodal Learning for Clinical Decision Support, D. Stoyanov, Z. Taylor, G. Carneiro, T. Syeda-Mahmood, A. Martel, L. Maier-Hein, J. M. R. Tavares, A. Bradley, J. P. Papa, V. Belagiannis, J. C. Nascimento, Z. Lu, S. Conjeti, M. Moradi, H. Greenspan, and A. Madabhushi, eds., Springer International Publishing, pp. 3–11.

[12] Babcock, D. A., Neto, L. T., Davis, Z., Karman-Shoemake, K., Woeber, C., Bajimaya, R., and MacManus, D., 2022. "Summary of the 5^{th} Propulsion Aerodynamics Workshop: Inlet cross-flow results". In AIAA SCITECH 2022 Forum, January 3-7, 2022, San Diego, CA & Virtual, no. AIAA 2022-0814, pp. 1–26.

[13] AIAA Inlets, Nozzles & Propulsion Systems Integration Technical Committee, 2021. 5^{th} AIAA propulsion aerodynamics workshop. `https://paw.larc.nasa.gov/wp-content/uploads/sites/83/2020/08/PAW5_Inlet_Participant_Guide.pdf`. Accessed: 2021-12-22.

[14] Murphy, J. P., and MacManus, D. G., 2011. "Ground vortex aerodynamics under crosswind conditions". *Experiments in Fluids,* ***50***(1), Jan, pp. 109–124.

[15] Zantopp, S., MacManus, D., and Murphy, J., 2010. "Computational and experimental study of intake ground vortices". *The Aeronautical Journal (1968),* ***114***(1162), p. 769–784.

[16] Murphy, J. P., and MacManus, D. G., 2011. "Intake ground vortex prediction methods". *Journal of Aircraft,* ***48***(1), pp. 23–33.

[17] Mishra, N., MacManus, D., and Murphy, J., 2012. "Intake ground vortex characteristics". *Proceedings of the Institution of Mechanical Engineers, Part G: Journal of Aerospace Engineering,* ***226***(11), pp. 1387–1400.

[18] Sayma, A. I., Vahdati, M., Sbardella, L., and Imregun, M., 2000. "Modeling of three-dimensional viscous compressible turbomachinery flows using unstructured hybrid grids". *AIAA Journal,* ***38***(6), pp. 945–954.

[19] Sayma, A. I., Vahdati, M., and Imregun, M., 2000. "An integrated nonlinear approach for turbomachinery forced response prediction. part I: formulation". *Journal of Fluids and Structures,* ***14***(1), pp. 87–101.

[20] Lee, K.-B., Wilson, M., and Vahdati, M., 2018. "Effects of Inlet Disturbances on Fan Stability". *Journal of Engineering for Gas Turbines and Power,* ***141***(5), 12. 051014.

[21] Sureshkumar, P., Lee, K.-B., Puente, R., and Stapelfeld, S., 2022. "Impact of the Spatial Arrangement of Inlet Distortions on Resonant Fan Response". In Proceedings of Global Power and Propulsion Society, no. GPPS-TC-2022-0132, pp. 1–16.

[22] Rao, A. N., Sureshkumar, P., Stapelfeldt, S., Lad, B., Lee, K.-B., and Rico, R. P., 2022. "Unsteady Analysis of Aeroengine Intake Distortion Mechanisms: Vortex Dynamics in Crosswind Conditions". *Journal of Engineering for Gas Turbines and Power,* ***144***(12), 10. 121005.

[23] Mishra, S., 2020. U-net—biomedical-image-segmentation. `https://github.com/sauravmishra1710/U-Net---Biomedical-Image-Segmentation`.

[24] Mishra, S., 2020. Brain-tumor-segmentation. `https://github.com/sauravmishra1710/UNet-Plus-Plus---Brain-Tumor-Segmentation`.

[25] Le, Q. T., and Ooi, C., 2021. "Surrogate modeling of fluid dynamics with a multigrid inspired neural network architecture". *Machine Learning with Applications,* ***6***, p. 100176.

[26] Hennigh, O., 2017. Automated design using neural networks and gradient descent.

[27] Ribeiro, M. D., Rehman, A., Ahmed, S., and Dengel, A., 2020. DeepCFD: Efficient steady-state laminar flow approximation with deep convolutional neural networks.